Published in final edited form as:
Magn Reson Med. 2010 May ; 63(5): 1230–1237. doi:10.1002/mrm.22306.

Respiratory and Cardiac Self-Gated Free-Breathing Cardiac CINE Imaging with Multi-Echo 3D Hybrid Radial SSFP Acquisition

Jing Liu, **Pascal Spincemaille**, **Noel C.F. Codella**, **Thanh D. Nguyen**, **Martin R. Prince**, and **Yi Wang**
Department of Radiology, Weill Cornell Medical College, New York, NY, United States

Abstract

A respiratory and cardiac self-gated free-breathing 3D cine SSFP imaging method using multi-echo hybrid radial sampling is presented. Cartesian mapping of the k-space center along the slice encoding direction provides intensity-weighted position information, from which both respiratory and cardiac motions are derived. With radial sampling in plane every TR, no extra scan time is required for sampling the k-space center. Temporal filtering based on density compensation is used for radial reconstruction to achieve high SNR and CNR. High correlation between the self-gating signals and external gating signals is demonstrated. This respiratory and cardiac self-gated free-breathing 3D radial cardiac cine imaging technique provides image quality comparable to that acquired with the multiple breath-hold 2D Cartesian SSFP technique in short axis, four chamber and two chamber orientations. Functional measurements from the 3D cardiac short axis cine images are found to be comparable to those obtained using the standard 2D technique.

Keywords

Self-gating; free breathing; k-space center; center of mass; multi-echo radial; 3D cardiac cine

INTRODUCTION

For volumetric coverage of the heart, clinically multiple slices are acquired using 2D SSFP sequence during multiple breath-holds. However, breath-holding positions may vary from slice to slice, causing slice misregistration (gaps or overlaps between successive slices). Patients may also have limited breath-holding capability (1), leading to motion artifacts. Clinical cardiac cine balanced steady-state free precession (SSFP) MR imaging requires electrocardiographic (ECG) gating to synchronize heart motion across multiple heartbeats. The external gating prolongs patient preparation and may become unreliable during scanning due to the magnetohydrodynamic interference. Thus methods without breath-holding and external ECG gating are desirable. In recent years, techniques by using acquired MR data for both respiratory and cardiac gating have been developed.

Respiratory position may be measured by acquiring MR signal from internal organs undergoing respiratory motion such as the diaphragmatic navigator (NAV) (2,3) and k-space centers (4–8), or by using the image data itself (9,10). NAV gating often performs well for free-breathing 3D coronary artery imaging where data are acquired during a limited portion of cardiac cycle, but is not suited for cine SSFP imaging due to the interruption of the steady state. K-space center gating methods have been applied to free-breathing respiratory self-

Contact information: Yi Wang, Cornell MRI, 416 East 55th Street, New York, NY, 10022, USA, Phone: 212-752-3936, Fax: 212-421-1844, yiwang@med.cornell.edu.

gated coronary (4,5,7) as well as cine (6,8) imaging. Respiratory gating by using the image data requires image reconstruction and registration calculation through the cardiac circle (9,10).

Cardiac gating signals have been obtained using extra navigator echoes (11–14) or image data (15). These cardiac self-gated methods typically use breath-holds to avoid the complexity of separating cardiac motion from respiratory motion. During free breathing, respiratory and cardiac motions superimpose but they occur at different frequencies and therefore can be separated with appropriate filters. Approaches without external respiratory or cardiac gating have been proposed for 2D human imaging (16–18), 2D mouse imaging (19,20) and 3D mouse imaging (21).

Compared to 2D imaging, 3D imaging provides thinner slices and contiguous volume coverage without slice misregistration errors (22) and is a better imaging method for accurate volume measuring and post-processing. 3D imaging also generates higher signal-to-noise ratio (SNR), although blood-to-myocardium contrast-to-noise ratio (CNR) may be lower due to reduced flow enhancement effect associated with large volume imaging (23). In this study, we present a free-breathing 3D cine imaging method using hybrid radial sampling with both respiratory and cardiac self-gating (24). Motion is detected using the center of mass of the projection of the imaging volume onto the slice encoding direction, which is repeatedly acquired during radial scanning without any extra data sampling. Radial sampling also provides the advantage of achieving high in-plane resolution and temporal resolution by using temporal filtering (sliding window or view sharing) (25). An approximately uniform dynamic imaging view order in which each projection acquired only once is achieved with a golden ratio based sampling scheme (26). The developed respiratory and cardiac self-gated free-breathing 3D cine imaging technique was compared with the standard 2D breath-hold cine imaging in terms of SNR, CNR, contrast and the functional parameters of the left ventricle.

METHODS

Data acquisition

A previously developed stack of multi-echo radial samplings with a Cartesian slice encoding and radial sampling in the k_x-k_y plane was adapted for 3D cardiac cine imaging (27). Multi-echo radial sampling maximizes data acquisition efficiency by acquiring data throughout the entire readout gradient including dephaser and rephaser gradients (28). The multi-echo 3D hybrid radial sampling pattern together with the view ordering scheme are shown in Figure 1a. All slice encodes for a given projection angle are acquired sequentially before switching to the next projection angle. The projection angle is incremented by $180°/\gamma = 111.2°$, where γ is the golden ratio (1.618) to give perpetually distinct projection angles during scanning (26). This interleaving view order provides approximately uniform k-space sampling at any time point, allowing for robust sliding window reconstructions, and for variable temporal resolution and arbitrary duration reconstructions (26). Note that radial acquisition samples the in-plane (k_x-k_y) k-space center every TR, and the sequential slice encoding samples the k_z axis ($k_x = k_y = 0$) every n_zTR, where n_z is the number of slice encodes.

Extraction of self-gating signals

The slice encoded k_x-k_y centers (acquired once per cardiac phase) were Fourier transformed into the image space to obtain the projection of the imaging volume onto the k_z axis. Figure 1b shows a record of the projection profiles, illustrating the temporal signal variations due to respiratory and cardiac motions. The motion signal was derived as the center of mass of this projection, which is the average z position weighted by signal intensity (Figure 1c) (4). The

changes in this z intensity-weighted position (ZIP) include both respiratory and cardiac motions that occur during the data acquisition. Since these motions are known to have different frequency contents (0.1–0.5 Hz for respiratory motion and 0.6–3 Hz for cardiac motion) (18), they can be separated by filtering according to the frequency bands (Figure 1d&e). This filtering is an iterative process starting with initial rates, e.g. a respiratory rate of 14 bpm (0.23 Hz) and a heart rate of 60 bpm (1 Hz). Local maximum (peak) and minimum (valley) of the extracted motion signals were detected based on these initial rates and were used to update the rates. A few iterations of this process generate robust motion filtering and peak/valley detection.

Self-gating image reconstruction

Given the detected respiratory and cardiac motions, the respiratory and cardiac phase associated with each data segment was determined. Because the R-R interval varies during the long data acquisition, the number of cardiac phases for cine image reconstruction was chosen based upon the most frequent R-R interval. Cardiac cycles that were 30% longer or shorter than this interval were not used for image reconstruction in order to suppress the effects of arrhythmia and any self-gating errors. Furthermore, a respiratory histogram was calculated (Figure 2) and only data acquired within a given window (i.e., 50% of acquired data) around the peak of the histogram were used for image reconstruction.

When multiple coil elements were used, the coil element with the smallest variance of the detected R-R intervals was selected for cardiac gating, and similarly the coil element with the smallest variance of respiratory peak or valley positions was chosen for respiratory gating.

With the double gating scheme, the interleaved projections assigned to each cardiac phase were less likely to be uniformly distributed, which increased the undersampling artifacts. To reduce these artifacts, a temporal filtering technique based on the calculation of k-space sampling density compensation was applied (25). A temporal function for each cardiac phase controls how much high-frequency k-space data from adjacent phases was utilized. In theory this can be designed by following the cardiac gating pattern of one cycle, which corresponds to the correlation between the cardiac phases. In this study, a simple linear decay function was used.

Human scans

Cardiac imaging was performed in seven normal volunteers (5 men and 2 women, mean age of 30.8 years ± 6.9 standard deviation [SD]) using a 1.5T GE HDx scanner (33 mT/m maximum gradient amplitude, 120 mT/m/s slew rate). The study was approved by the local institutional review board and informed consent was obtained from all subjects prior to imaging. An eight-channel cardiac phased-array coil was used for signal reception.

Respiratory and cardiac self-gated multi-echo 3D hybrid radial SSFP images of the left ventricle (LV) were acquired in the standard short-axis (SA), two-chamber (2C) and four-chamber (4C) views during free breathing. Typical imaging parameters were as follows: TR = 4.4 ms, TE = 0.3/1.6/2.9 ms, flip angle = 40°, FOV = 32–34 cm, image matrix = 256 × 256, readout bandwidth = ±125 kHz, slice thickness = 10 mm (SA) and 8 mm (2C and 4C), number of slices = 10–14 (SA) and 8 (2C and 4C). The number of partial slice encodes was 10 to allow greater slab coverage without sacrificing temporal resolution. Temporal resolution was 44 ms (SA) and 35 ms (2C and 4C). Both ECG and respiratory bellows signals within the scan were recorded for comparison purposes.

For comparison, routine breath-hold 2D cine images were also obtained in the SA view using the following typical imaging parameters: TR = 3.5 ms, TE = 1.2 ms, flip angle = 60 °,

readout bandwidth = ±125 kHz, FOV = 34 cm, image matrix = 256 × 256, slice thickness = 6 mm, slice gap = 4 mm, number of slices = 12–14, views per segment = 20, number of reconstructed cardiac phases = 28. Total 2D acquisition time was about 5 minutes including resting periods between breath-holds. Total free-breathing 3D acquisition time was approximately 5 minutes to match the total breath-hold 2D acquisition time.

Data analysis

External gating signals (ECG and bellows signals) were compared with the self-gating signals over the five subjects with available external gating data. The correlation coefficient between external and self-gating signals was calculated as $\frac{E\{[x-E(x)][y-E(y)]\}}{\sqrt{E\{[x-E(x)]^2\}}\sqrt{E\{[y-E(y)]^2\}}}$, where $E(\cdot)$ is the expected value operator. The time indexes of the detected ECG and respiratory triggers were also compared.

Image sharpness obtained during breath-hold and free breathing with different respiratory gating windows was evaluated on the LV cavity-myocardium interface over seven subjects. Eight signal profiles evenly spaced around the LV circumference and positioned across the endocardial border were measured from mid-LV images acquired during end-diastole and end-systole. The local maximum (I_{max}) and minimum (I_{min}) intensity values across the endocardial border were determined, from which image sharpness was calculated as the inverse of the distance between $0.8(I_{max}-I_{min})+I_{min}$ and $0.2(I_{max}-I_{min})+I_{min}$ (9). The image sharpness of each subject was obtained by averaging over the eight profiles.

Functional measurements including LV end-diastolic volume (LVEDV), LV end-systolic volume (LVESV), LV ejection fraction (LVEF), and LV end-diastolic mass (LVEDM) were calculated for both 2D and 3D cine acquisitions using a fully automated myocardial segmentation algorithm called LV Myocardial Effusion Threshold Reduction with Intravoxel Computation (LV-METRIC) (29). Seven subjects were studied. Linear regression and Bland-Altman analysis was used to assess the agreement between measurements obtained with 2D and 3D imaging methods. All data are expressed as mean ± standard deviation (SD).

A two-tailed paired-sample t-test was used to test the difference between the 2D and 3D methods with p-value of less than 0.05 considered as statistically significant.

RESULTS

Figure 3 shows an example of the detected cardiac and respiratory self-gating signals as well as the recorded ECG and respiratory bellows gating signals in one subject, demonstrating good correlation. The correlation between the cardiac self-gating triggers and the ECG triggers was excellent, with a correlation coefficient of 1.00 ± 0 and a linear regression slope of 1.00 ± 0. However, there was a delay of 273.4 ± 20.7 ms from the ECG trigger to the cardiac self-gating trigger. The respiratory self-gating signals also correlated well with the respiratory bellows (0.82 ± 0.1 correlation coefficient). The delay between the respiratory self-gating triggers and the bellows triggers (corresponding to detected valley positions) was 631.5 ± 230.8 ms. The cardiac cycle duration (RR) was 974 ± 176 ms and the respiratory cycle duration was 4149± 356 ms. The standard deviations of delay between the self-gating and external triggers were 20.7 ms (cardiac) and 230.8 ms (respiratory), demonstrating rather small beat-to-beat and breath-to-breath variability with respect to the average RR interval and the respiratory period, respectively.

Figure 4 shows representative short-axis LV images acquired with the proposed self-gated free-breathing 3D cine method. Note that a very narrow respiratory gating window (20% of the acquired data) produced major streaking artifacts due to undersampling (Figure 4a) and very large gating windows (75% and 100%) led to motion blurring of myocardial borders, papillary muscles, and surrounding epicardial fat (Figure 4c&d). Accordingly, a 50% respiratory gating window was chosen to balance between undersampling and motion artifacts (Figure 4b). Further improvement in image quality (higher SNR and reduced streaking) could be obtained with temporal filtering (Figure 4e).

Image sharpness (here referring to the left ventricular endocardium) obtained with different respiratory gating windows is presented in Table 1. Maximum image sharpness was obtained with approximately 50% gating window during both end-systole and end-diastole, and sharpness degraded somewhat as the gating window was increased or decreased from this optimal range. Utilization of the temporal filtering improved the image sharpness. Compared to breath-hold 2D imaging, self-gated 3D imaging with 50% gating window provided slight lower but statistically different image sharpness for end-diastole ($p = 0.01$), while the image sharpness is similar for end-systole ($p = 0.14$).

Figures 5 and 6 demonstrate comparable cine image quality obtained with self-gated free-breathing 3D imaging and breath-hold 2D imaging in the basal, mid and apical SA views, as well as 4C and 2C views. Note that 3D images have slight blurring due to residual breathing motion artifact and lower blood-to-myocardium contrast due to reduced flow enhancement effect associated with thick volume imaging.

Figure 7 shows the reformatted cardiac four-chamber view obtained from breath-hold 2D short-axis images. Note the slice misregistration error along the septum, which was not present in the reformatted four-chamber view obtained with 3D imaging.

Comparison of the LV functional measurements is shown in Figure 8 and summarized in Table 2, demonstrating excellent correlation and narrow limits of agreements between breath-hold 2D and self-gated free-breathing 3D cine acquisitions. Note that the difference in all LV functional parameters between 2D and 3D imaging was not statistically significant ($p>0.05$).

DISCUSSION

In this study, a respiratory and cardiac self-gated free-breathing 3D cardiac cine imaging method with multi-echo radial acquisition was demonstrated to provide similar image quality and comparable LV functional parameters to that obtained with the standard breath-hold 2D acquisition. The respiratory and cardiac self-gating signals were found to be highly correlated with the respiratory bellows and ECG signals, respectively, suggesting good motion sensitivity. The proposed technique was capable of tracking both respiratory and cardiac motions and provided effective motion suppression for various cardiac imaging orientations, including the standard SA, 2C and 4C views. This eliminates the need for ECG electrodes and permits free-breathing acquisitions without requiring extra scan time for motion detection.

Our proposed technique is robust against motion artifacts due to the acquisition scheme that acquires radial sampling trajectories in-plane (k_x-k_y) (30) at perpetually distinct angles and that traverses all slice encodes repeatedly. Compared to the projection sampling with constant sequential angle increments during scanning, the golden ratio based projection view order allows robust and flexible time-resolved reconstruction and is suitable for real-time imaging. Especially with the double gating scheme, the constant sequential angle view order

has less uniform angle distribution for generating cine images, compared to the golden ratio view order.

A 2D radial self-gating technique has been proposed for mouse imaging by using the k-space center point at echo time for gating (19). However, gradient delays and eddy current errors may cause the derived gating signal to depend on the projection angles, making it a less sensitive or less consistent measure of motion (19). With our acquisition sequence, three k-space center points at different echo times were acquired per TR. In this study, we only used the first k-space center signal acquired when the radial trajectory starts at the k-space center in order to avoid gradient delays and eddy current errors.

Usually different coils were optimal for tracking respiratory motion and cardiac motion respectively. While only individual coils were used for either respiratory or cardiac gating, a combination of more or of all coils may provide more motion information and should be the subject of further study.

For bright blood cardiac imaging, the variation in the k-space center data mainly originates from the changes in blood volume when the heart contracts and relaxes, and from bulk motion of the whole heart due to respiration. If the whole subject moves within the FOV and there is no blood volume change, then the k-space center magnitude ($k_x=k_y=k_z=0$) does not change. Unless the object moves only along k_x-k_y plane, which may not occur for the typical heart orientations used in clinical practice, ZIP will always catch a displacement. ZIP gating is expected to be more robust than using a single k-space center point (31).

The current gating temporal resolution matches the image reconstruction temporal resolution n_zTR, while it can be improved up to TR by applying a sliding window to the k-space centers acquired through time. Image reconstruction can also achieve the same resolution with higher reconstruction computation cost. Current computation (not optimized) in MatLab (The MathWorks, Natick, MA, USA) required 12 minutes per phase on a 2.8 GHz MacBook.

Median positions of the peak and valley positions of the self respiratory gating signal, plotted as solid lines in Figure 2 (left), were used to provide a robust range for calculating the step size of the position histogram.

Figure 3a suggests that the cardiac self-gating signal corresponds to the change of the heart blood volume. The cardiac self-gating signal has a minimum (valley) at the end of systole (according to the ECG signal), when the contracted heart has minimal volume. This behavior was observed in all cases.

The quantitative measurements of sharpness presented in Table 1 showed that the image sharpness degraded as the respiratory gating window became large (75%, 100%). However, a low gating window (20%) generated poor image quality and harmed the image sharpness. Utilization of the temporal filtering not only reduced artifacts, but also improved the image sharpness. Free-breathing imaging with minimized motion provided lower image sharpness compared with breath-hold imaging.

The respiratory self-gating window was chosen to be 50% to balance the competing effect of streaking artifact (with too narrow gating windows) and motion blurring (with too wide gating windows) (Figure 4). All the cases have been examined to verify this choice as a good balance. Temporal filtering was more powerful in removing streaking artifacts for subjects with lower heart rates, for which each cardiac phase was assigned a smaller number of projections, given a fixed total scan time of five minutes.

3D imaging generally provides higher SNR than 2D imaging due to longer scan time. However, saturation of the blood magnetization due to the thick slab excitation of 3D imaging reduces the inflow effect, so blood SNR and blood-to-myocardium CNR usually degrades when compared to 2D imaging (23,32). 3D radial imaging may also have lower SNR and CNR compared to 2D Cartesian imaging due to streaking artifacts presented as background noise. Because of the difficulty of noise estimation in the presence of these streaking artifacts, SNR and CNR measurements were excluded from this study.

The 3D slices at the edge of the slab have lower blood to myocardium contrast than the central slices due to imperfect slice profile, which may be improved by using a better RF pulse. 3D cardiac cine imaging can be performed after the injection of Gadolinium contrast agent to improve the contrast between the blood and myocardium, for instance immediately before the delayed contrast enhanced imaging of the heart.

The 2D multiple breath-hold method is usually used as the gold standard, however it suffers from slice misregistration and hence has limited accuracy in cardiac chamber volume quantification. Three-dimensional echocardiography (ECHO) has been shown to be accurate and reproducible for cardiac function measurements (33). However, ECHO data were not available for the volunteers in this preliminary study.

There are several technical possibilities for further improving image quality. Similar to applying the temporal filtering along the cardiac phases, filtering could be performed along the respiratory motion direction as well in order to further reduce undersampling artifacts. The purpose of the respiratory gating is to maximize data efficiency within a certain motion tolerance. Motion correction may be implemented to improve image quality (10,34). Recently, many parallel imaging methods have been proposed to accelerate the image acquisition and would in all likelihood further reduce the scan time in this study by a factor of at least two.

In conclusion, free-breathing 3D cine SSFP imaging is achieved with simultaneous respiratory and cardiac self-gating at different imaging orientations (short axis, four chamber and two chamber views). An excellent correspondence between the self-gating and external gating triggers is demonstrated. The 3D short axis cine imaging with the proposed technique provides image quality and functional measurements comparable to those acquired with the multiple breath-hold 2D Cartesian SSFP technique.

Acknowledgments

This work was supported in part by NIH R01 HL064647.

References

1. Jahnke C, Paetsch I, Achenbach S, Schnackenburg B, Gebker R, Fleck E, Nagel E. Coronary MR imaging: breath-hold capability and patterns, coronary artery rest periods, and beta-blocker use. Radiology. 2006; 239(1):71–78. [PubMed: 16493014]
2. Wang Y, Rossman PJ, Grimm RC, Riederer SJ, Ehman RL. Navigator-echo-based real-time respiratory gating and triggering for reduction of respiration effects in three-dimensional coronary MR angiography. Radiology. 1996; 198(1):55–60. [PubMed: 8539406]
3. Peters DC, Nezafat R, Eggers H, Stehning C, Manning WJ. 2D free-breathing dual navigator-gated cardiac function validated against the 2D breath-hold acquisition. J Magn Reson Imaging. 2008; 28(3):773–777. [PubMed: 18777547]
4. Stehning C, Bornert P, Nehrke K, Eggers H, Stuber M. Free-breathing wholeheart coronary MRA with 3D radial SSFP and self-navigated image reconstruction. Magn Reson Med. 2005; 54(2):476–480. [PubMed: 16032682]

5. Lai P, Larson AC, Bi X, Jerecic R, Li D. A dual-projection respiratory self-gating technique for whole-heart coronary MRA. J Magn Reson Imaging. 2008; 28(3):612–620. [PubMed: 18777542]
6. Uribe S, Muthurangu V, Boubertakh R, Schaeffter T, Razavi R, Hill DL, Hansen MS. Whole-heart cine MRI using real-time respiratory self-gating. Magn Reson Med. 2007; 57(3):606–613. [PubMed: 17326164]
7. Lai P, Larson AC, Park J, Carr JC, Li D. Respiratory self-gated four-dimensional coronary MR angiography: a feasibility study. Magn Reson Med. 2008; 59(6):1378–1385. [PubMed: 18506786]
8. Spincemaille P, Nguyen TD, Prince MR, Wang Y. Kalman filtering for real-time navigator processing. Magn Reson Med. 2008; 60(1):158–168. [PubMed: 18581354]
9. Larson AC, Kellman P, Arai A, Hirsch GA, McVeigh E, Li D, Simonetti OP. Preliminary investigation of respiratory self-gating for free-breathing segmented cine MRI. Magn Reson Med. 2005; 53(1):159–168. [PubMed: 15690515]
10. Leung AO, Paterson I, Thompson RB. Free-breathing cine MRI. Magn Reson Med. 2008; 60(3): 709–717. [PubMed: 18727100]
11. Spraggins TA. Wireless retrospective gating: application to cine cardiac imaging. Magn Reson Imaging. 1990; 8(6):675–681. [PubMed: 2266792]
12. White RD, Paschal CB, Clampitt ME, Spraggins TA, Lenz GW. Electrocardiograph-independent, “wireless” cardiovascular cine MR imaging. J Magn Reson Imaging. 1991; 1(3):347–355. [PubMed: 1802148]
13. Crowe ME, Larson AC, Zhang Q, Carr J, White RD, Li D, Simonetti OP. Automated rectilinear self-gated cardiac cine imaging. Magn Reson Med. 2004; 52(4):782–788. [PubMed: 15389958]
14. Schulz J, Korn M, Deimling M, Semmler W, Bock M. Flow-compensated self-gating. MAGMA. 2008; 21(5):307–315. [PubMed: 18668271]
15. Larson AC, White RD, Laub G, McVeigh ER, Li D, Simonetti OP. Self-gated cardiac cine MRI. Magn Reson Med. 2004; 51(1):93–102. [PubMed: 14705049]
16. Kim WS, Mun CW, Kim DJ, Cho ZH. Extraction of cardiac and respiratory motion cycles by use of projection data and its applications to NMR imaging. Magn Reson Med. 1990; 13(1):25–37. [PubMed: 2319933]
17. Wang Z, Willett CG, Yin FF. Reduction of organ motion by combined cardiac gating and respiratory gating. Int J Radiat Oncol Biol Phys. 2007; 68(1):259–266. [PubMed: 17321071]
18. Buehrer M, Curcic J, Boesiger P, Kozerke S. Prospective self-gating for simultaneous compensation of cardiac and respiratory motion. Magn Reson Med. 2008; 60(3):683–690. [PubMed: 18727084]
19. Hiba B, Richard N, Janier M, Croisille P. Cardiac and respiratory double self-gated cine MRI in the mouse at 7 T. Magn Reson Med. 2006; 55(3):506–513. [PubMed: 16463350]
20. Hiba B, Richard N, Thibault H, Janier M. Cardiac and respiratory self-gated cine MRI in the mouse: comparison between radial and rectilinear techniques at 7T. Magn Reson Med. 2007; 58(4):745–753. [PubMed: 17899593]
21. Brinegar C, Wu YJ, Foley LM, Hitchens T, Ye Q, Ho C, Liang ZP. Real-time cardiac MRI without triggering, gating, or breath holding. Conf Proc IEEE Eng Med Biol Soc. 2008; 2008:3381–3384. [PubMed: 19163434]
22. Swingen C, Seethamraju RT, Jerosch-Herold M. An approach to the three-dimensional display of left ventricular function and viability using MRI. Int J Cardiovasc Imaging. 2003; 19(4):325–336. [PubMed: 14598902]
23. Nezafat R, Herzka D, Stehning C, Peters DC, Nehrke K, Manning WJ. Inflow quantification in three-dimensional cardiovascular MR imaging. J Magn Reson Imaging. 2008; 28(5):1273–1279. [PubMed: 18972337]
24. Liu, J.; Spincemaille, P.; Nguyen, N.; Block, FW.; Prince, MR.; Wang, Y. Respiratory and cardiac self-gated free-breathing cardiac CINE imaging with multi-echo 3D hybrid radial acquisition. Proceedings of the 17th Annual Meeting of ISMRM; Honolulu. 2009. p. 2239
25. Liu J, Redmond MJ, Brodsky EK, Alexander AL, Lu A, Thornton FJ, Schulte MJ, Grist TM, Pipe JG, Block WF. Generation and visualization of four-dimensional MR angiography data using an undersampled 3-D projection trajectory. IEEE Trans Med Imaging. 2006; 25(2):148–157. [PubMed: 16468449]

26. Winkelmann S, Schaeffter T, Koehler T, Eggers H, Doessel O. An optimal radial profile order based on the Golden Ratio for time-resolved MRI. IEEE Trans Med Imaging. 2007; 26(1):68–76. [PubMed: 17243585]
27. Liu, J.; Wieben, O.; Reeder, SB.; Block, WF. Multi-echo 3D Hybrid Radial SSFP Cardiac CINE Imaging for Whole Heart Coverage in a Single Breathhold. Proceedings of the 15th Annual Meeting of ISMRM; Berlin. 2007. p. 3868
28. Lu A, Brodsky E, Grist TM, Block WF. Rapid fat-suppressed isotropic steady-state free precession imaging using true 3D multiple-half-echo projection reconstruction. Magn Reson Med. 2005; 53(3):692–699. [PubMed: 15723411]
29. Codella NC, Weinsaft JW, Cham MD, Janik M, Prince MR, Wang Y. Left ventricle: automated segmentation by using myocardial effusion threshold reduction and intravoxel computation at MR imaging. Radiology. 2008; 248(3):1004–1012. [PubMed: 18710989]
30. Glover GH, Pauly JM. Projection reconstruction techniques for reduction of motion effects in MRI. Magn Reson Med. 1992; 28(2):275–289. [PubMed: 1461126]
31. Spincemaille, P.; Liu, J.; Nguyen, TD.; Prince, MR.; Wang, Y. Self-navigator for free-breathing 3D SSFP cardiac imaging: center of mass along the slice direction versus the image signal sum using the center of k-space. Proceedings of the 17th Annual Meeting of ISMRM; Honolulu. 2009. p. 4626
32. Peters DC, Ennis DB, Rohatgi P, Syed MA, McVeigh ER, Arai AE. 3D breath-held cardiac function with projection reconstruction in steady state free precession validated using 2D cine MRI. J Magn Reson Imaging. 2004; 20(3):411–416. [PubMed: 15332248]
33. Gopal AS, Shen Z, Sapin PM, Keller AM, Schnellbaecher MJ, Leibowitz DW, Akinboboye OO, Rodney RA, Blood DK, King DL. Assessment of cardiac function by three-dimensional echocardiography compared with conventional noninvasive methods. Circulation. 1995; 92(4): 842–853. [PubMed: 7641365]
34. Gai N, Axel L. Correction of motion artifacts in linogram and projection reconstruction MRI using geometry and consistency constraints. Med Phys. 1996; 23(2):251–262. [PubMed: 8668107]

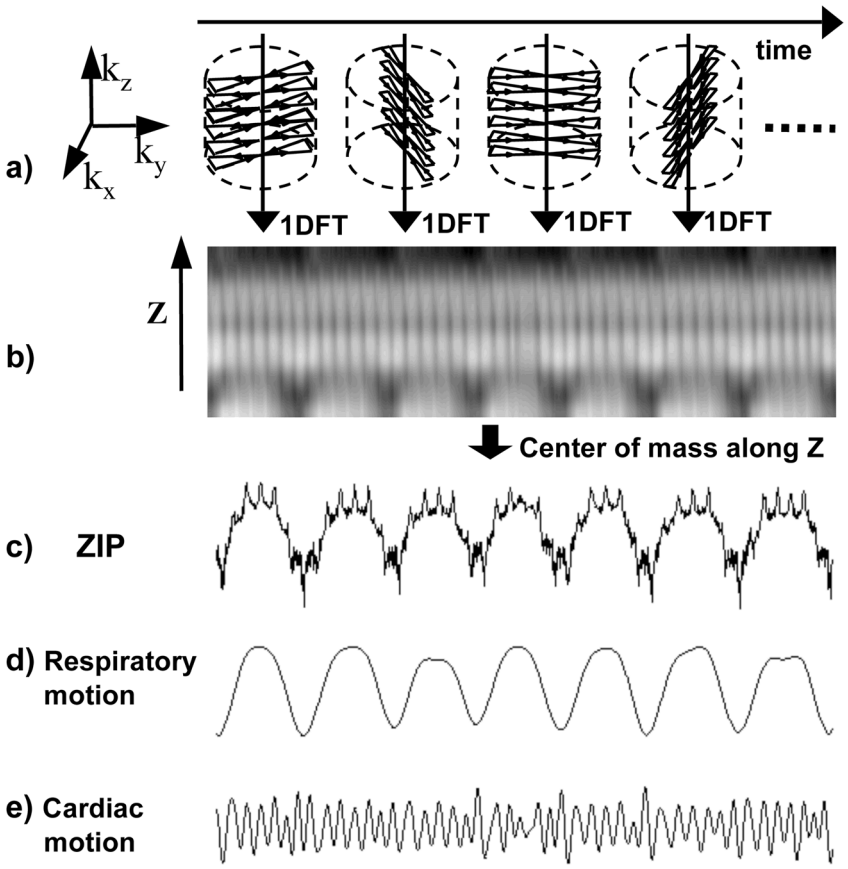

Figure 1.
Respiratory and cardiac self-gating signals were derived from the center of mass of the z-intensity profile in multi-echo hybrid 3D radial imaging. a) k-space sampling trajectories, b) z-intensity profile evolving over time, c) center of mass of b) along z, d) respiratory motion, e) cardiac motion.

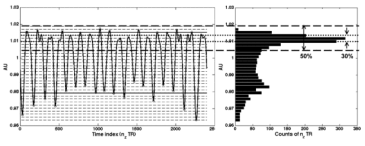

Figure 2.

The respiratory gating was determined based on the histogram of the respiratory motion signal. Sampling projections were divided into multiple bins according to the position of the respiratory motion (left). A histogram (right) was generated for employing a respiratory gating window, such as 30% (dotted line) and 50% (dashed line). Note that the gating windows are expressed as the fraction of the total amount of the acquired data.

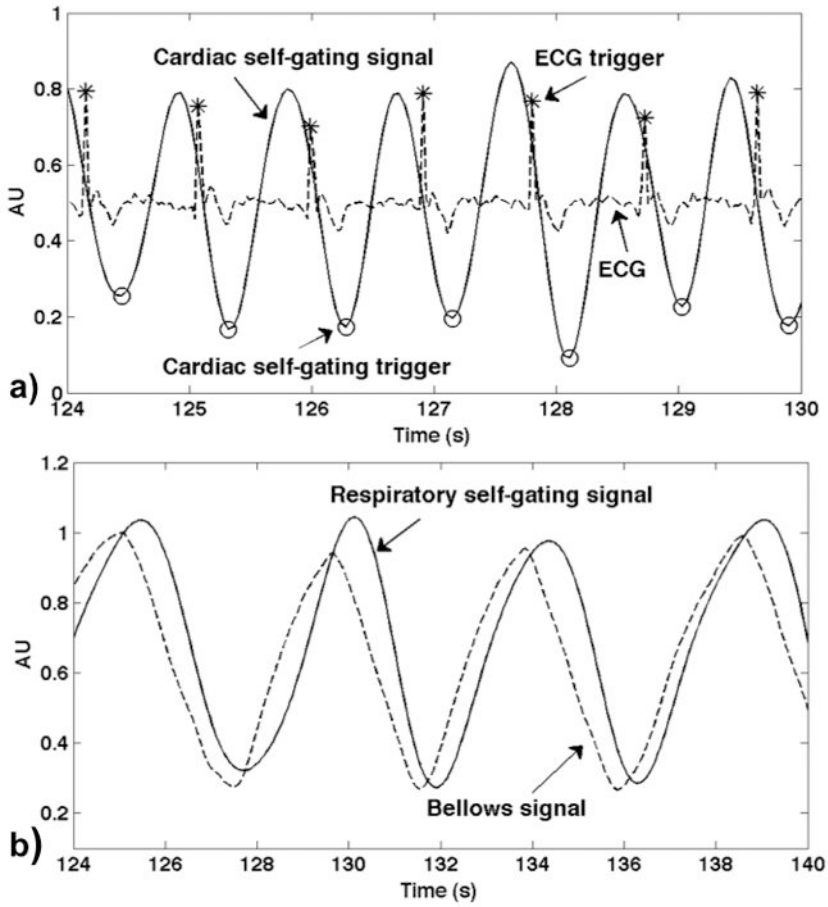

Figure 3.

Respiratory and cardiac self-gating signals were compared with bellows and ECG signals. Cardiac self-gating (solid line) and ECG (dashed line) signals were synchronized in a), presented by stars and circles, respectively. Respiratory self-gating (solid line) and bellows (dashed line) signals were synchronized in b). Amplitudes of all curves were rescaled for display purposes only.

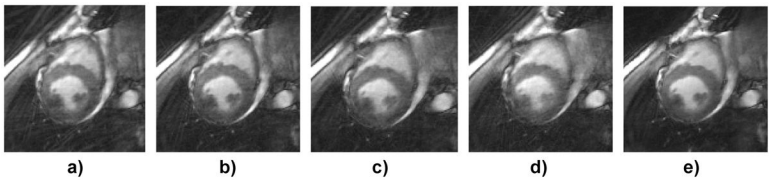

Figure 4.
Short axis views acquired with respiratory and cardiac self-gated free-breathing 3D technique were compared by using different respiratory gating windows: a) 20%, b) 50%, c) 75%, d) 100%, and e) 50% with temporal filtering. Data were acquired in a healthy volunteer with a heart rate of 75 bpm and a respiratory rate of 11 bpm. Images at end systole are shown.

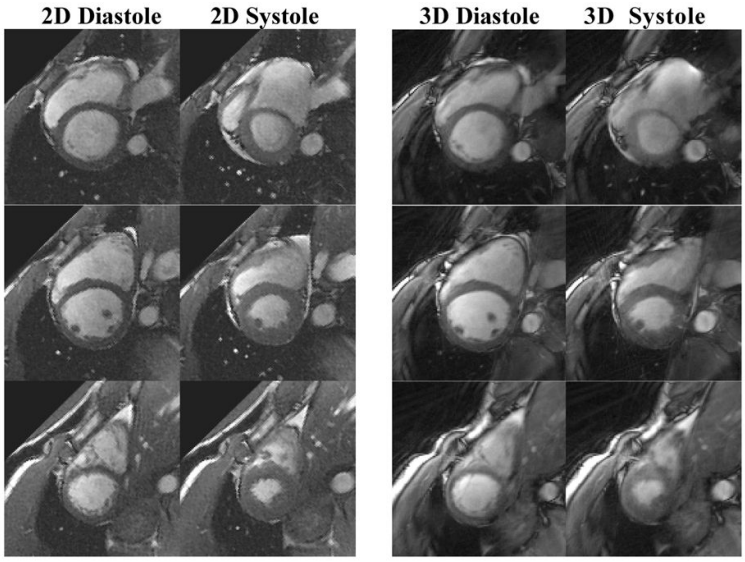

Figure 5.
Short axis cine images obtained with the proposed self-gated free-breathing 3D technique (right block) were compared with those with ECG-gated multiple breath-hold 2D technique (left block). Data were acquired from a healthy volunteer with a heart rate of 53 bpm and a respiratory of 19 bpm. Images of three representative slices (rows) at end diastole and end systole are shown. A temporal filter and a respiratory gating window of 50% was used for the 3D results.

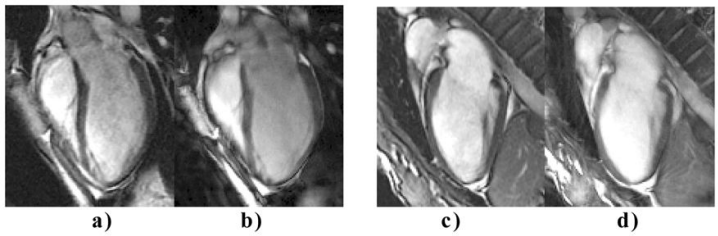

Figure 6.
Four-chamber (left block) and two-chamber views (right block) obtained with ECG-gated breath-hold 2D technique a)c) and the proposed self-gated free-breathing 3D technique b)d) are shown.

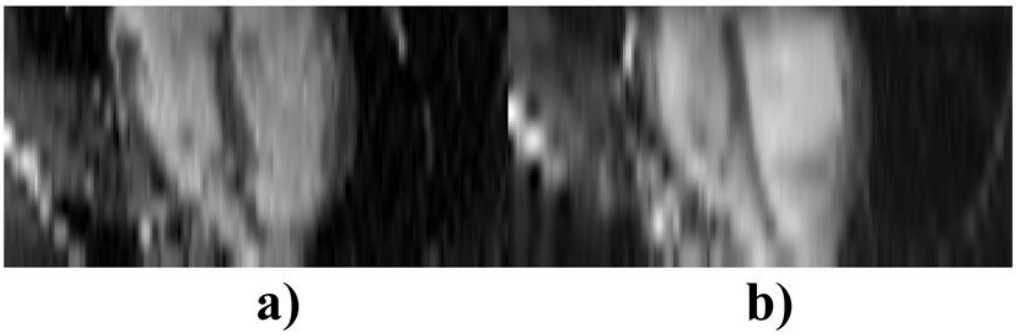

Figure 7.
Reformatted four-chamber views of the standard 2D and the proposed 3D short axis images were compared. The multiple breath-hold 2D imaging a) suffered slice misregistration errors, which were not presented in 3D imaging, b).

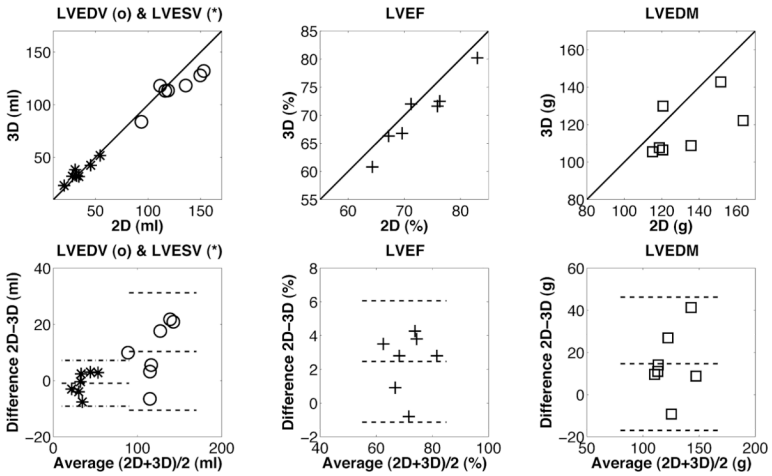

Figure 8.

Comparisons of functional measurements obtained with the standard 2D method and the proposed self-gated 3D technique are presented. The first row exhibits the LVEDV, LVESV, LVEF, and LVEDM measurements of the two techniques, with the 2D measurements along the horizontal axis and 3D measurements along the vertical axis. The second row shows the Bland-Altman plots of those measurements. The dashed lines show the mean bias and the confidence interval.

Table 1

Comparison of sharpness of LV cavity-myocardium interface acquired with the proposed self-gated free-breathing 3D imaging using various respiratory gating windows and the standard breath-hold 2D imaging.

mm^{-1}	3D 20%	3D 50%	3D 75%	3D 100%	3D 50% with temporal filtering	2D breath-hold
End Diastole	0.43 ± 0.06	0.44 ± 0.07	0.44 ± 0.06	0.42 ± 0.06	0.45 ± 0.05	0.54 ± 0.06
End Systole	0.40 ± 0.07	0.42 ± 0.06	0.41 ± 0.07	0.40 ± 0.07	0.44 ± 0.03	0.48 ± 0.06

Table 2

Left ventricular functional measurements obtained with standard breath-hold 2D imaging and the proposed self-gated free-breathing 3D imaging.

	LVEDV (ml)	LVESV (ml)	LVEF (%)	LVEDM (g)
2D	118.4 ± 19.0	31.3 ± 7.7	73.7 ± 5.2	122.2 ± 18.0
3D	112.4 ± 24.7	31.8 ± 6.1	71.0 ± 6.2	115.4 ± 20.1
bias	6.1 ± 8.9	−0.5 ± 2.7	2.7 ± 3.5	6.8 ± 14.1
p-value	0.12	0.65	0.09	0.25